RESEARCH ARTICLE

{M}acro-molecular
Bioscience
www.mbs-journal.de

Check for updates

Studying Activated Fibroblast Phenotypes and Fibrosis-Linked Mechanosensing Using 3D Biomimetic Models

Francesca Paradiso, Marcos Quintela, Stefania Lenna, Stefano Serpelloni, David James, Sergio Caserta, Steve Conlan, Lewis Francis, and Francesca Taraballi*

Fibrosis and solid tumor progression are closely related, with both involving pathways associated with chronic wound dysregulation. Fibroblasts contribute to extracellular matrix (ECM) remodeling in these processes, a crucial step in scarring, organ failure, and tumor growth, but little is known about the biophysical evolution of remodeling regulation during the development and progression of matrix-related diseases including fibrosis and cancer. A 3D collagen-based scaffold model is employed here to mimic mechanical changes in normal (2 kPa, soft) versus advanced pathological (12 kPa, stiff) tissues. Activated fibroblasts grown on stiff scaffolds show lower migration and increased cell circularity compared to those on soft scaffolds. This is reflected in gene expression profiles, with cells cultured on stiff scaffolds showing upregulated DNA replication, DNA repair, and chromosome organization gene clusters, and a concomitant loss of ability to remodel and deposit ECM. Soft scaffolds can reproduce biophysically meaningful microenvironments to investigate early stage processes in wound healing and tumor niche formation, while stiff scaffolds can mimic advanced fibrotic and cancer stages. These results establish the need for tunable, affordable 3D scaffolds as platforms for aberrant stroma research and reveal the contribution of physiological and pathological microenvironment biomechanics to gene expression changes in the stromal compartment.

1. Introduction

The extracellular matrix (ECM) plays crucial roles during many physiological processes such as organism development, tissue repair, and organ homeostasis.[1] A reciprocal interaction between cellular and matrix components, defined as "dynamic reciprocity,"[2] has been shown to orchestrate both normal physiological function and disease development. Pathological conditions in any organ tissue, such as chronic or repeated injuries and irritation, can lead to a failure to heal and subsequent tissue fibrosis,[1] a dysregulated outcome of the tissue repair response following injury.[3]

The ECM of fibrotic tissue is characterized by increased collagen and fibronectin synthesis,[4] while local tissue fibroblasts become activated and increase their contractility and secretion of inflammatory mediators.[5] In a physiological setting, these changes initiate the wound healing response. When damage is minor or nonrepetitive, a transient increase in the deposition of ECM components supports

F. Paradiso, S. Lenna, S. Serpelloni, F. Taraballi
Center for Musculoskeletal Regeneration, Houston Methodist Academic Institute
Houston Methodist Research Institute
6670 Bertner Ave, Houston, TX 77030, USA
E-mail: ftaraballi2@houstonmethodist.org

F. Paradiso, M. Quintela, D. James, S. Conlan, L. Francis
Reproductive Biology and Gynaecological Oncology Group
Swansea University Medical School
Singleton Park, Swansea, Wales SA28PP, UK

F. Paradiso, S. Lenna, S. Serpelloni, F. Taraballi
Orthopedics and Sports Medicine
Houston Methodist Hospital
6445 Main St, Houston, TX 77030, USA

S. Caserta
Department of Chemical Materials and Industrial Production Engineering
University of Naples Federico II
P.zzle Tecchio 80, Naples 80125, Italy

**ADVANCED
SCIENCE NEWS**
www.advancedsciencenews.com

Macro-
molecular
Bioscience
www.mbs-journal.de

efficient wound healing and restoration of functional tissue homeostasis. However, when the injury is repetitive or severe, ECM components accumulate excessively, with consequent tissue architecture disruption, organ dysfunction, and ultimately organ failure.[6,7] The resulting increase in matrix stiffness, traditionally viewed as an end point of organ fibrosis, is now recognized as a critical regulator of tissue fibrogenesis that promotes organ fibrosis, hijacking the normal physiologic wound-healing program.[8] ECM–cell interactions result in tensional, compressive, and shear forces that are translated into biochemical signaling through a process known as mechanotransduction,[9] and through this signaling, matrix stiffness controls a range of cell activities including migration, adhesion, phenotypic modulation, and survival[10] and can activate a "myofibroblast program" in fibroblastic cells.[11,12]

Matrix remodeling in fibrotic tissues is thought to be similar to that in the formation of premetastatic niches.[13] In many solid tumors, the formation of fibrotic tissue is referred as a desmoplastic response. Desmoplasia is a fibrotic state characterized by increased deposition, altered organization, and enhanced post-translational modifications of ECM proteins; chronic inflammation; fibroblast expansion and activation; and elevated angiogenesis, resembling many of the facets of chronic tissue fibrosis.[14] In the tumor context, matrix dysregulation is now considered a hallmark of solid tumors.[15] This process occurs in many advanced carcinomas, including breast cancer, and is responsible for the clinical presentation of a tumor as a "lump."[16–18] One area of intensive research is investigating how matrix remodeling that occurs in tumor settings, and the resulting tumor-associated tissue fibrosis, help to create an environment for primary and secondary tumor colonization of the tissue. Indeed, in some of the most well-studied tumor types like breast, pancreas, lung, and colon, tumor growth is usually associated with a dense fibrotic stroma and their aggressiveness is often associated with higher collagen levels and extensive dense, linearized, and cross-linked ECM in the tissue.[19–22] As a result, malignant tissue is typically stiffer than its normal counterpart, with studies showing that normal breast tissue is 20 times softer than its neoplastic counterpart.[23] Specifically, breast and pancreatic tumor stiffness has been exploited to detect cancer mass either by physical palpation or using imaging modalities such as magnetic resonance imaging, computerized tomography, or elastography.[24,25]

At a cellular level, pathological fibrosis is driven by a feedback loop in which the fibrotic ECM is both a cause and consequence of fibroblast activation, known as myofibroblasts or herein referred to as activated fibroblasts (AFs). The origin of myofibroblasts has been shown to be tissue dependent[26] and they can be activated by many stimuli such as reactive oxygen species, pathogen-released activators, and many other soluble molecules secreted by infiltrating cells.[27,28] Specifically, transforming growth factor-beta (TGFβ1) is a potent fibroblast activator, enhancing fibroblast contractile capacity, inducing the incorporation of smooth muscle α-actin (α-SMA) within cytoskeletal stress fibers, and increasing focal adhesion clustering, all of which represent a typical phenotype in fibrotic pathologies or aberrant wound healing.[29–31] In parallel, as a result of structural ECM changes, biomechanical signals are also thought to initiate and sustain tissue fibrosis.[9,32]

TGF-β1 is also thought to promote tumor initiation and progression.[33,34] In many solid tumors, reciprocal TGFβ1 signaling between cancer cells and the tumour microenvironment (TME) promotes cancer progression by activating fibroblasts into cancer-associated fibroblasts (CAFs).[35,36] CAFs usually exert a protumorigenic effect, enhancing tumor phenotype and promoting tumor growth, cancer cell proliferation, angiogenesis, invasion, and metastasis.[37–39] Indeed, fibroblasts adjacent to the tumor express genes mainly related to stress and inflammation,[40] and as observed in breast cancer, macrophage dysfunction can enhance the process of inflammation, contributing to metastasis.[41] Resulting from CAF activation and consequent production of a dense connective tissue, such altered biomechanical properties often induce tumor metastasis, angiogenesis, and hypoxia.[42,43]

In line with this, cultivating tumor stromal cells in 3D systems can allow more in-depth investigations by fully recapitulating the cell–matrix interactions observed in tumor tissue. Precise 3D scaffold fabrication enables the production of tissue-like materials, closely mimicking native tissues for various applications, from regenerative medicine to cancer research.[44–50] Exploiting porous scaffold collagen-based material, we investigate stiffness effects on both normal fibroblasts' (NFs) and AFs cellular migration, morphology, functionality, and gene expression profiles. In this study, we characterize the mechanical properties of a tunable collagen-based 3D in vitro model to fully replicate both soft/physiological and stiff/fibrotic-like tissue. The present work further establishes the advantages of 3D modeling and the tuning properties of porous scaffolds while establishing a foundation for further exploration of the role of the stroma in fibrotic/desmoplastic tissue responses. As such, it represents a meaningful and reliable platform to combine biological and biophysical cues in a 3D system, envisioning a stroma-ECM model for drug discovery, personalized medicine, and basic research of pathologies characterized by the dysregulation of ECM homeostasis.

2. Results

2.1. Scaffold Characterization

As one of the main components of interstitial matrix, collagen type I is an elective biomaterial used in in vitro scaffold model development.[51] As collagen crosslinking can influence tissue strength and elasticity, we exploited two strategies, using different percentages of the cross linker 1,4-butanediol diglycidyl ether (BDDGE) to specifically reproduce the mechanical features of both native and dense fibrotic tissue.[43,52] Various percentages of BDDGE were tested (data not shown) to determine the final conditions, where 1% BDDGE was chosen to mimic tumor-fibrotic/stiff tissue (St) and 0.01% to mimic normal/benign/soft tissue (So).

Scaffold mechanics were analyzed at the nanoscale using atomic force microscopy (AFM), showing a 36-fold increase in stiffness between St (144.58 $\pm$ 0.010 kPa) and So (4.35 $\pm$ 0.005 kPa) ($p < 0.05$; **Figure 1**A and Figure S1A, Supporting Information). Shear rheometry was used to calculate the average mechanical parameters for the bulk scaffolds,[53] in

**ADVANCED
SCIENCE NEWS**

www.advancedsciencenews.com
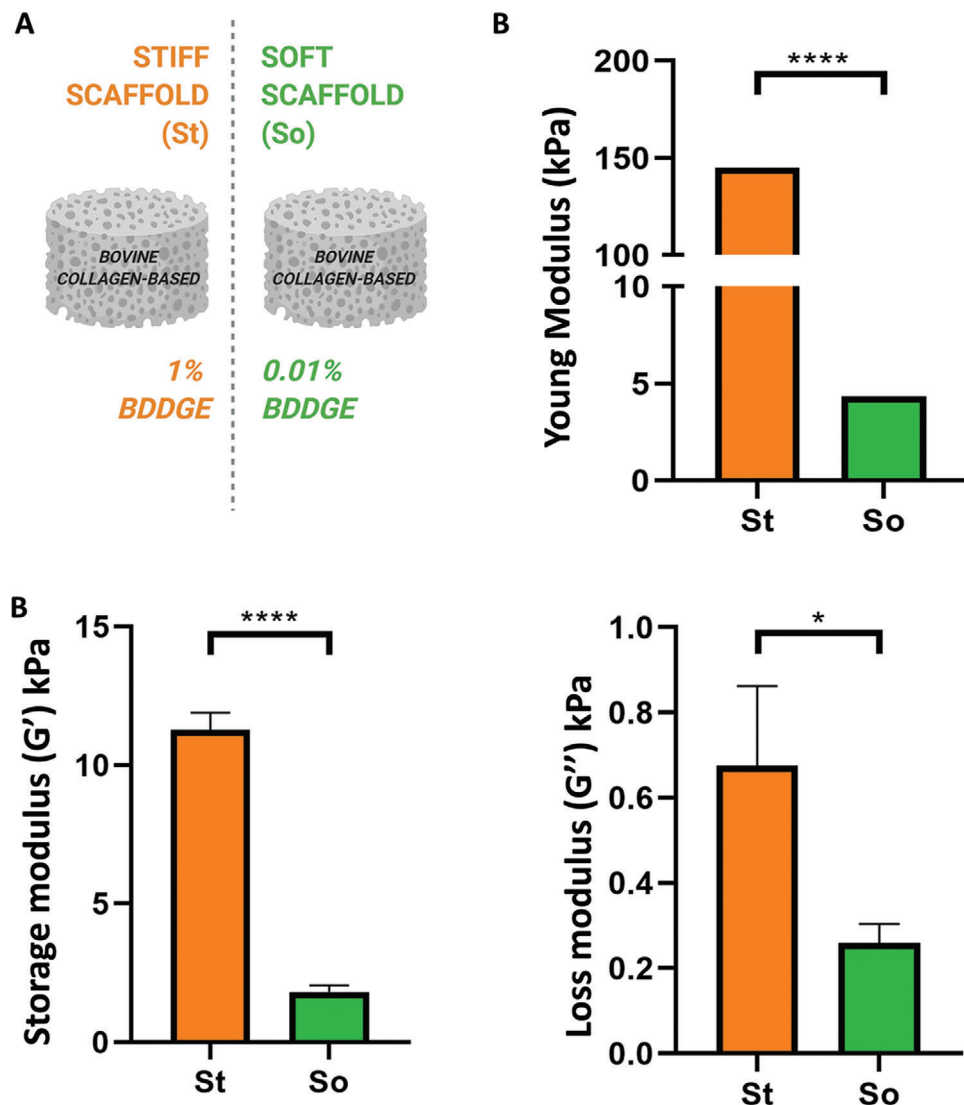
{M} acro-
olecular
Bioscience

www.mbs-journal.de

Figure 1. Mechanical features of native normal/cancer tissue are mimicked in a 3D collagen-based in vitro system, using different percentage of crosslinker 1,4-butanediol diglycidyl ether (BDDGE). A) Atomic force microscopy analysis of Young modulus (kPa) in St and So scaffolds. B) Rheology analysis of storage modulus (G', kPa) and loss modulus (G'', kPa) in St and So scaffolds. Data are mean + standard deviation ($n = 3$). T-test with Welch's correction, ****$p < 0.0001$, *$p < 0.05$. Illustration made with Biorender.

order to characterize the elastic, elastoplastic, and viscous flow behavior of both St and So at the tissue scale (see Figure S1B,C, Supporting Information). St storage modulus and loss modulus at 1 Hz (11.271 ± 0.619 and 0.67 ± 0.187 kPa, respectively) were significantly increased compared to those of So (1.816 ± 0.24 and 0.259 ± 0.043 kPa, respectively) (Figure 1B), indicating greater viscoelasticity of St compared to So scaffolds.

Furthermore, the scaffold tan δ was analyzed as G''/G', and both scaffolds showed values less than 1, confirming their solid-like behavior. St scaffolds showed lower tan δ (0.06 ± 0.003) compared to So (0.14 ± 0.008), indicating a greater ability of the So material to absorb energy and relieve stress when compared to the St material (Figure S1D, Supporting Information). Analysis of scanning electron microscopy (SEM) images of both So and St showed the typical porous structure of a 3D sponge scaffold (**Figure 2**A). Porosity measurements showed that St scaffolds ex-

hibited an average pore size of 5000 ± 400 μm^2, corresponding to an average diameter of 80 μm, compared to an average So pore size of 2564 ± 698 μm^2 and an average diameter of 57 μm (Figure 2B; $p < 0.05$), with comparable pore circularity (Figure 2B).

Fourier transform infrared spectroscopy (FTIR) and thermogravimetric analysis (TGA) were used to characterize scaffold composition after crosslinking. FTIR spectral analysis for both St and So showed that the amide I (1700–1600 cm^{-1}), amide II (1600–1500 cm^{-1}), and amide III ($\approx$1200–1300 cm^{-1}) peaks, which constitute the characteristic signature of collagen material, were reported in both St and So sample profiles, with no significant differences observed (Figure 2C). Similarly, no significant difference was observed between St and So samples using TGA analysis. Both materials underwent endothermic reaction at around 100 °C (evaporation of the water moisture present in the material), while thermal transition and material degrada-

**ADVANCED
SCIENCE NEWS**

www.advancedsciencenews.com
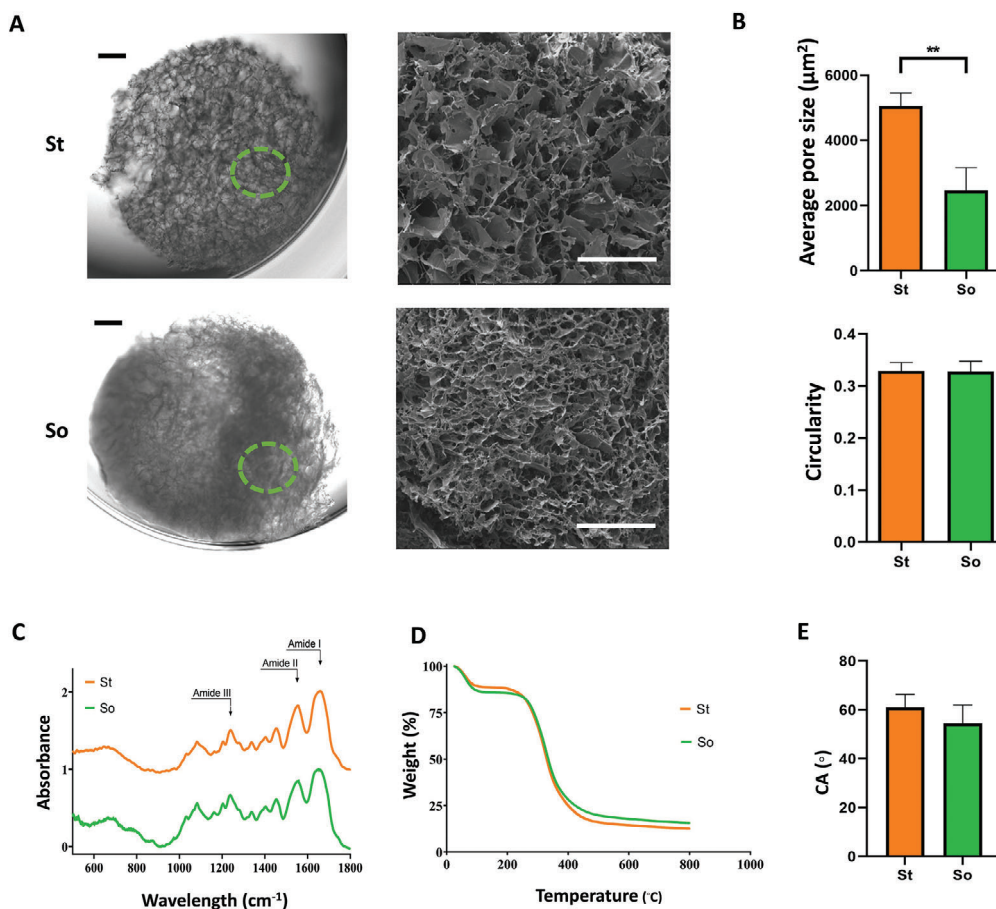
Macro-
olecular
Bioscience

www.mbs-journal.de

Figure 2. St scaffolds showed higher average pore sizes, but same composition and hydrophilic properties compared to So. A) Bright-field images of whole scaffolds (left) and SEM magnification of the scaffolds (right). B) SEM analysis of average pore size (μm^2) and circularity. *T*-test with Welch's correction, **p < 0.01. C) FTIR spectra of St and So scaffolds. The spectra highlighted the presence of typical collagen Amide I, Amide II, Amide III. D) Thermo gravimetric Analysis (TGA). E) Water contact angle (WCA) measurements. *T*-test with Welch's correction, **p < 0.01.

tion happened after 200 °C of the heating ramp, for both samples (Figure 2D). Finally, to validate scaffold suitability for cell seeding, contact angle (CA) measurements were used, showing both scaffolds had hydrophilic properties (CA < 90°), with no significant differences observed between the two materials (Figure 2E).

2.2. Normal Fibroblasts are Activated into Activated Fibroblasts by TGFβ1 and Both Colonize the Scaffold Matrix

In order to develop a ubiquitous model to study NF and AF response to stiffness within the 3D model and assess the suitability of the 3D collagen scaffolds for stromal studies, human fetal lung fibroblast cells (MRC5) cells were used and were activated into AFs using a dose range of TGFβ1. Expression levels of known AF markers, *fibroblast activation protein (FAP)*, and *α-SMA*, were first monitored in 2D cell cultures after TGFβ1 treatment. Flow cytometry and western blot analysis showed an increase of FAP (Figure S2A, Supporting Information) and α-SMA expression (Figure S2B, Supporting Information) following treatment with 25 and 50 ng mL^{-1} TGFβ1, compared to the untreated

control. Similarly, and as expected, the relatively high doses of 25 and 50 ng mL^{-1} of TGFβ1 were optimal for NF to AF activation in our 3D setting (Figure S3A,B, Supporting Information[54]).

MRC5 cells (±TGFβ1) were seeded on St and So scaffolds to determine if both NFs and AFs could attach, grow, and colonize the differential mechanical scaffolds. Cell death was monitored after seeding in 2D and 3D (St and So) for 7 d, using calcein/ethidium bromide staining, and assessed by flow cytometry (**Figure 3**A) and epifluorescence microscopy (Figure 3C). When analyzed quantitatively for viability, NFs and AFs were both viable, exhibiting calcein-positive staining on both St (NFs: 84% ± 7.2%, AFs: 87.3% ± 6.1%) and So (NFs: 81% ± 6.4, AFs: 84.3% ± 6.9) (Figure 3A). When treated with TGFβ1 in 3D, NFs showed increased gene expression of both FAP and ACTA2 (α-SMA) compared to those cultured in 2D, highlighting the substrate dimensionality effect on fibroblast activation (Figure 3B). Significant increases were observed in ACTA2 (α-SMA) (3.8-fold) and FAP (4.6-fold) expression following treatment with 25 ng mL^{-1} of TGFβ1 (*p* < 0.05). Similar increased expression of ACTA2 (α-SMA) (2.7-fold) and FAP (2.5-fold) were observed when treated with 50 ng mL^{-1} of TGFβ1 (Figure 3B). Both NF and AFs were able to penetrate and colonize the So and St scaffolds, as reported
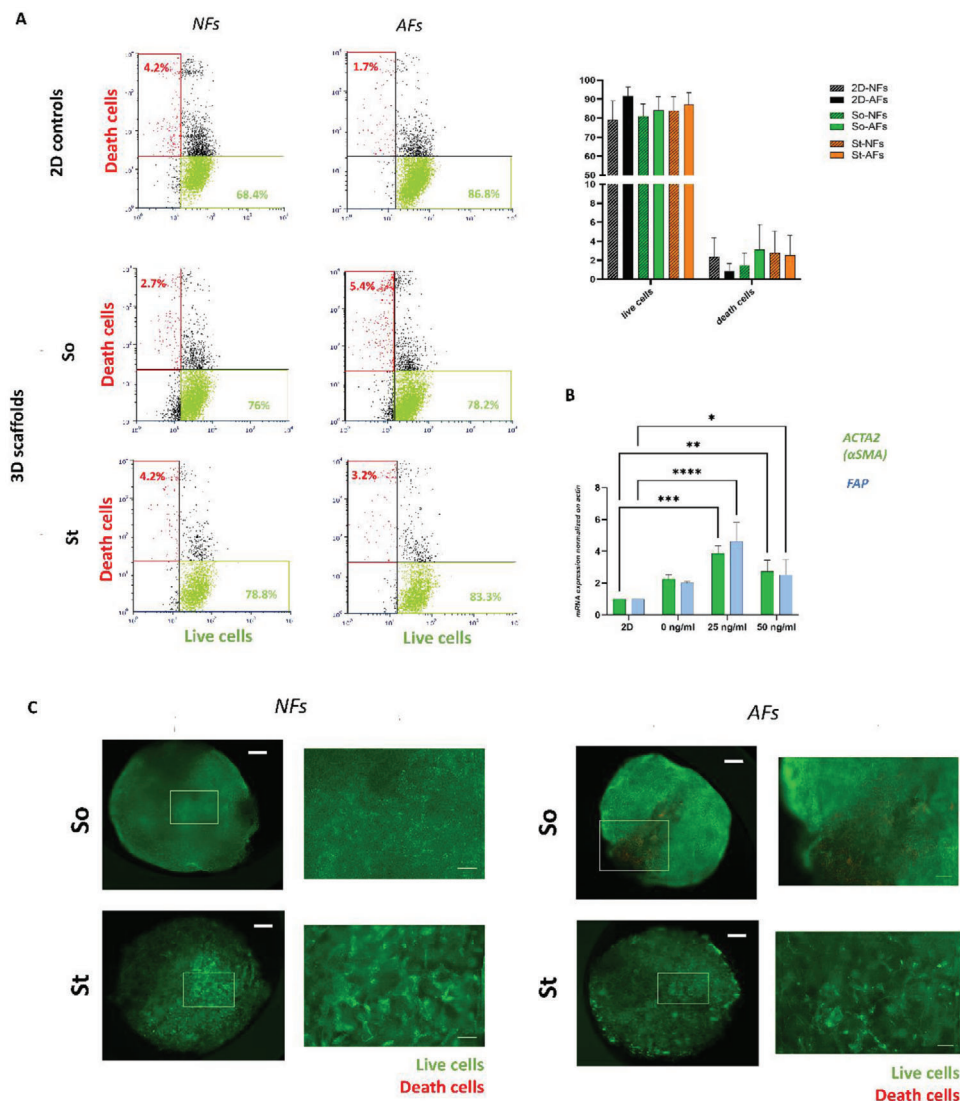
ADVANCED
SCIENCE NEWS
www.advancedsciencenews.com

[M]acro-
olecular
Bioscience
www.mbs-journal.de

Figure 3. NFs/AFs were viable and proliferated on both St and So scaffolds. A) Representative plots of cell live/death staining analyzed with flow cytometry and statistical analysis. B) ACTA2 (αSMA) and FAP mRNA expression under 0–50 ng mL^{-1} TGFβ1 treatment. Data normalized on 2D control. Data are mean + standard deviation ($n = 3$). D) Cell live/death staining analyzed with fluorescence microscopy. Analysis and imaging were performed after 7 d of culture. Scale in images of whole scaffold: 500 µm, scale in magnified images: 100 µm. Data are mean + standard deviation ($n = 3$).

by the 3D maximum intensity projection of three layers per scaffold collected (i.e., top, center, bottom) (Figure 3C).

2.3. Normal Fibroblast and Activated Fibroblast Migration and Morphology in Altered Mechanical Environments

The fibroblast migration pattern and length were then evaluated on 3D scaffolds, using live cell confocal imaging analysis of NFs and AFs cultured in 3D over 24 h, at an average depth of 800 µm for each scaffold (**Figure 4**A). Rendered movement tracking showed that AF directionality in So scaffolds followed a specific pattern, converging toward the center of the scaffold, while NFs had more random motility, with no specific direction (Figure 4A left). Conversely, NFs and AFs grown on St scaffolds

showed very few and short movements (Figure 4A right). Overall, the migration path of both NFs and AFs grown in St scaffolds was significantly decreased in both track length and displacement compared to So (Figure 4B; $p < 0.05$), suggesting an impairment of cell migration on the stiff material. Cellular morphology was also impacted by substrate stiffness, with both NF and AFs showing statistically higher cell circularity when cultured on St materials (Figure 4B), in part explaining the limited motility. To investigate if these phenotypic effects resulted in a modified collagen fiber alignment, we computationally analyzed collagen orientation from different areas of the scaffold using a Fluo View 3000 confocal microscope after 7 d of culture. The predominant orientation, for both NF and AFs, was around 0° among all the So samples, whereas the orientation was shifted to mostly −45° and 45° in both cell types on the St materials. Interestingly, AFs on St
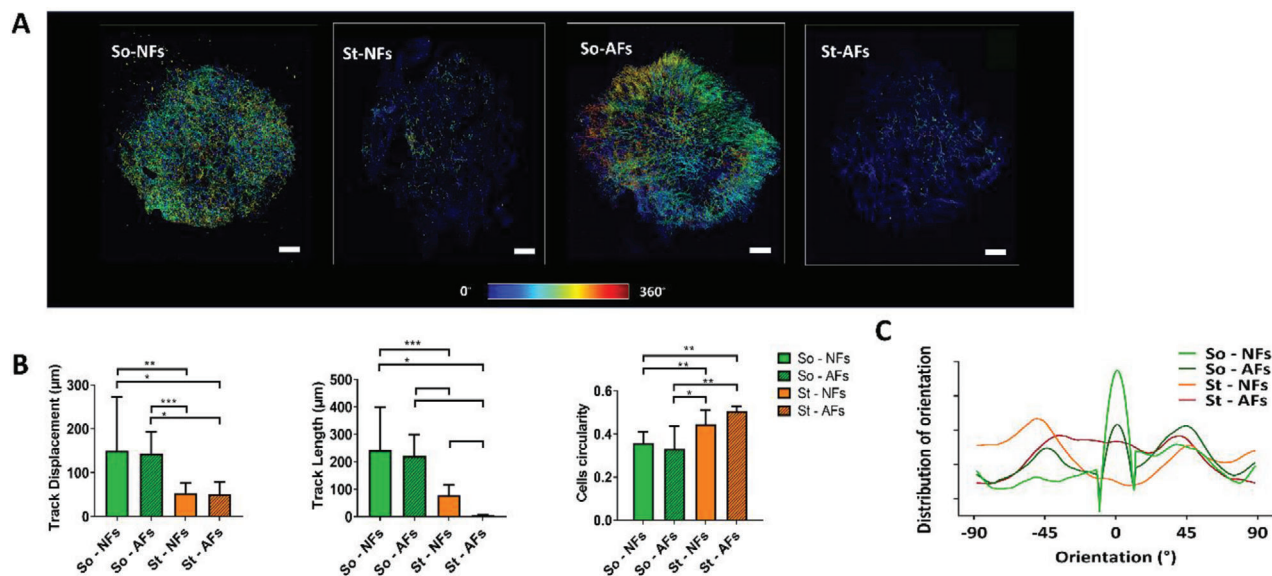
ADVANCED
SCIENCE NEWS
www.advancedsciencenews.com

[M] acro-
olecular
Bioscience
www.mbs-journal.de

Figure 4. NFs and AFs grown on St scaffolds showed shorter migration distance across scaffold and higher cell circularity compared to those on So. A) Live imaging rendering of the whole 3D scaffold (800 µm height) of NFs and AFs grown on St and So scaffolds from day 3 to day 4. Migratory tracks are shown using a rainbow scale. Scale bar: 600 µm. B) Track length (in µm), track displacement (µm), and cell circularity were analyzed using cellSens software. C) Collagen orientation analysis at 7 d of culture. Data are mean + standard deviation of 30 areas, $*p < 0.05$, $**p < 0.01$, $***p < 0.001$, $****p < 0.0001$.

scaffolds showed a hybrid pattern with a prevalent distribution between −45° and 45° and no predominant direction (Figure 4C and Figure S4, Supporting Information). These data, alongside the rounded phenotype and reduced track length and displacement, support the inactivity of AFs on this stiffer scaffold.

To correlate these phenotypes with cell cycle and proliferation, we utilized propidium iodide to quantify DNA content in our cell cultures (Figure S3C, Supporting Information). Using DNA content analysis to assess the cell cycle state of the cell, a higher number of cells in the G1 and S phases was observed in 2D compared to 3D, with no significant differences observed between NFs and AFs grown on So and St scaffolds. To confirm that the higher transition of G1→S phases for synthesis of DNA in 2D is in preparation for cell division and subsequent mitosis,[55] we assessed proliferation using CellTracker Green 5-chloromethylfluorescein diacetate (CMFDA) staining (Figure S3D, Supporting Information). Overall, fibroblasts in 2D presented a slightly higher number of cell generations (up to generation 8) compared to 3D. No significant difference in number of generations was reported with this analysis.

2.4. Scaffold Remodeling and Stiff Substrate-Promoted Mechanotransduction

To test fibroblasts' contraction activity and ability to remodel their collagen scaffold environment, we recorded diameter changes over 7 d in culture. The shrinking effect on both So and St scaffolds was recorded from day 3 with live cell imaging (**Figure 5**A top), demonstrating that both NFs and AFs actively contract the So matrix between days 3 and 4 of culture (Videos from S1–S4, Supporting Information). Starting at 4 to 7 d of culture, scaffold

shrinkage was higher in So scaffolds culture with AFs compared to NFs (NFs/AFs : day 4 5512.4 µm ± 130.5/3884.3 µm ± 158.9; day 5 4739.6 µm ± 420.5/3921.6 µm ± 17.9; day 6 4546.5 µm ± 612.4/3363.9 µm ± 72.1; day 7 4345.4 µm ± 655.1/3341 µm ± 151.4) demonstrating the susceptibility of So materials to remodeling as well as higher contractility function of AFs compared to NFs in So scaffolds. No significant change in St scaffolds shrinkage was recorded for either NF or AF cells after 7 d (Figure 5A). Neither NFs or AFs showed an ability to promote St collagen scaffold contraction between days 3 and 4 (Videos S1–S4, Supporting Information, calcein-only staining and multiview).

Furthermore, H&E staining suggested that the effect of So scaffold shrinking is a denser matrix after 7 d compared to St (Figure S5, Supporting Information). Utilizing rheology, we evaluated whether the recorded macroscopic changes in scaffold diameter resulted in changed physical properties after 7 d of culture. A significant decrease in the So material storage modulus was observed at day 7 when cultured with NFs or AFs, compared to both empty scaffold (So D0) and So scaffold on day 1 (So-NFs vs D0; $p < 0.05$; Figure 5B). No changes were observed in St elastic properties (Figure 5C; $p > 0.05$). No significant variation was observed in scaffold material loss modulus for either So or St scaffolds (Figure 5C right; $p > 0.05$), further highlighting the plasticity of the softer So material to remodeling and the suitability of rheology analysis to test bulk tissue mechanic of fresh biological samples.

In order to test if Yes-associated protein 1 (YAP1) related mechanosignaling is upregulated in our models, YAP/Transcriptional co-activator with PDZ binding motif (TAZ) was assessed at the mRNA level in NF and AF cells in both the So and St scaffolds, compared to those in 2D. Specific
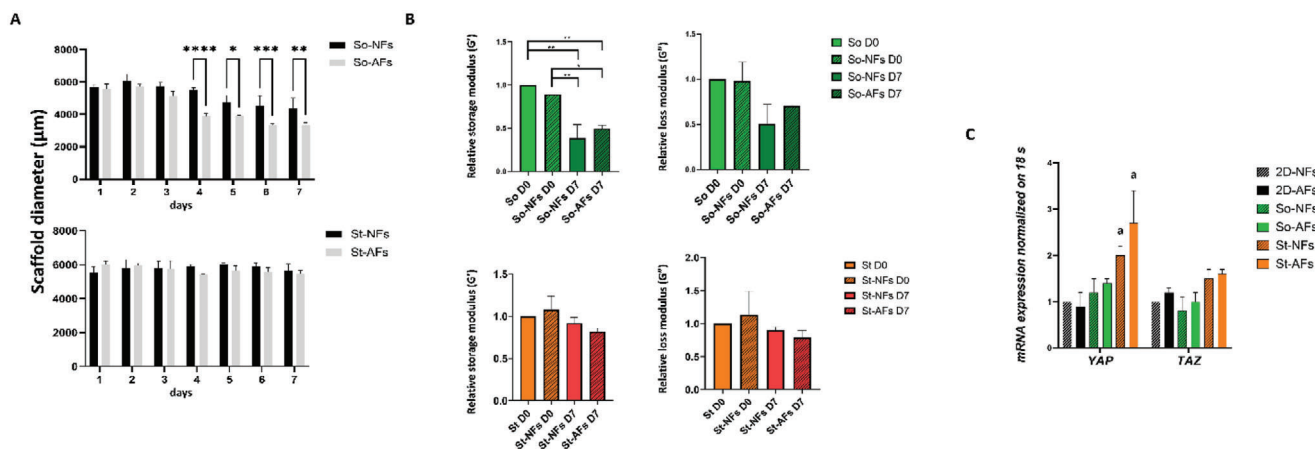
**ADVANCED
SCIENCE NEWS**

www.advancedsciencenews.com

Macro-
olecular
Bioscience

www.mbs-journal.de

Figure 5. So scaffolds are prone to remodeling by NFs and AFs but mechanotransduction is activated only on St scaffolds. A) Scaffold diameter analysis over 7 d of culture of NFs and AFs on So scaffolds (top) and St scaffolds (bottom). Data are mean + standard deviation ($n = 3$). B) Rheology analysis of storage modulus (G', left) and loss modulus (G'', right) in St and So scaffolds. Data normalized to D0 controls. Data are mean + standard deviation ($n = 3$). T-test with Welch's correction, $**p < 0.01$, $*p < 0.05$. C) Mechanosensing-related genes (yap-taz) mRNA expression in NFs and AFs at day 7 of culturing on 2D, So scaffolds, and St scaffolds. Data normalized to 2D control-NFs. Data are mean + standard deviation ($n = 3$).

activation of the mechanosensitivity pathways was observed on St scaffolds, demonstrated by increasing expression of YAP1 (Figure 5C).

2.5. Mechanistic Understanding and Transcriptome Analysis

We reported different AF cell behavior between So and St substrates; the So material stimulated AF migration and matrix reorganization resulting in scaffold shrinkage, while the St scaffold promoted AF mechanosensing seemingly resulting in impaired AF migratory properties and contractile functionality. To investigate these distinct AF phenotypes and understand mechanistic differentiation in terms of gene expression profiling, we conducted transcriptome-wide RNA-seq on AFs grown in 3D on So and St scaffolds after 7 d, using 2D culture of both NF and AF populations as relative controls.

Upon receipt of the raw files, we performed FastQC analyses were used to monitor the quality of the data. Phred scores are a measure of the accuracy of base calling from the sequencer. A Phred score of 40 indicates that there is a 99.99% chance that the base was called correctly, and a score of 30 indicates a 99.9% chance that the base was called correctly. An average Phred score of greater than 30 is usually considered sufficient. All samples met this criterion (Table S1, Supporting Information). Statistics relating to mapping of reads to the genome are shown in Table S2 in the Supporting Information. For all samples, >80% of reads are uniquely mapped confirming the validity of the data.

Principal component analysis (PCA) provides information on the overall structure of the analyzed dataset. PCA clearly showed the generation of distinct clusters, suggesting that both substrate stiffness and TGFβ1 activation lead to distinct AF phenotype differentiation at the transcriptome level (**Figure 6**A). Good reproducibility was observed between biological replicates and the most significant separation between data sets was between the activated and not activated state of fibroblasts promoted by TGFβ1 treatment.

To confirm fibroblast activation under TGFβ1 treatment, regardless of the substrate, we looked at the TGFβ1 "core" transcriptomic profile, reporting all the genes in common between AFs grown among both 2D and 3D substrates (217 genes), confirming the expression of AF biomarkers including *FAP* and *ACTA2* (α-SMA) that are representative of TGFβ1-driven fibroblast activation (Figure S6, Supporting Information).

We next aimed to evaluate gene expression variations in response to changes in the microenvironment stiffness in both AFs and NFs. Referring to the whole dataset of gene expressed in 3D conditions, AFs showed a higher number of genes uniquely identifying St culturing conditions (1133, 6.3% of the total) compared to So (872, 4.9% of the total); while the highest number of uniquely identifying genes for NFs was found under So condition compared to St (1386, 7.5% and 899, 4.9% respectively) (Figure 6B). The core 3D transcriptome of both NFs and AFs cultured on St/So showed distinct and significant differences compared to their 2D cultured counterparts (Figure S7, Supporting Information). Remarkably, the number of upregulated genes in AFs cultured within the 3D scaffolds compared to the 2D substrate where higher than that observed in NFs (228 vs 110 upregulated genes), as shown in Figure S6A,B in the Supporting Information. When these gene lists were analyzed via pathway analysis for the key upregulated pathways, a number of AF-related pathways related to matrix remodeling and the acquisition of an active/contractile phenotype were identified, including degradation of the ECM and collagen formation; ECM structural constituents conferring tensile strength and response to mechanical stimuli; and pathways related to pathological situations like fibrosis and the inflammatory response (Figure S6A, Supporting Information).

To investigate the unique signature promoted by substrate stiffness, differential analysis was performed to highlight gene pathways expression variations among NFs and AFs cultured on St versus So. Our analysis reported few significantly upregulated and down regulated genes for NFs between St versus So culture (76 upregulated and 90 downregulated; $p < 0.05$; Figure 6C), but
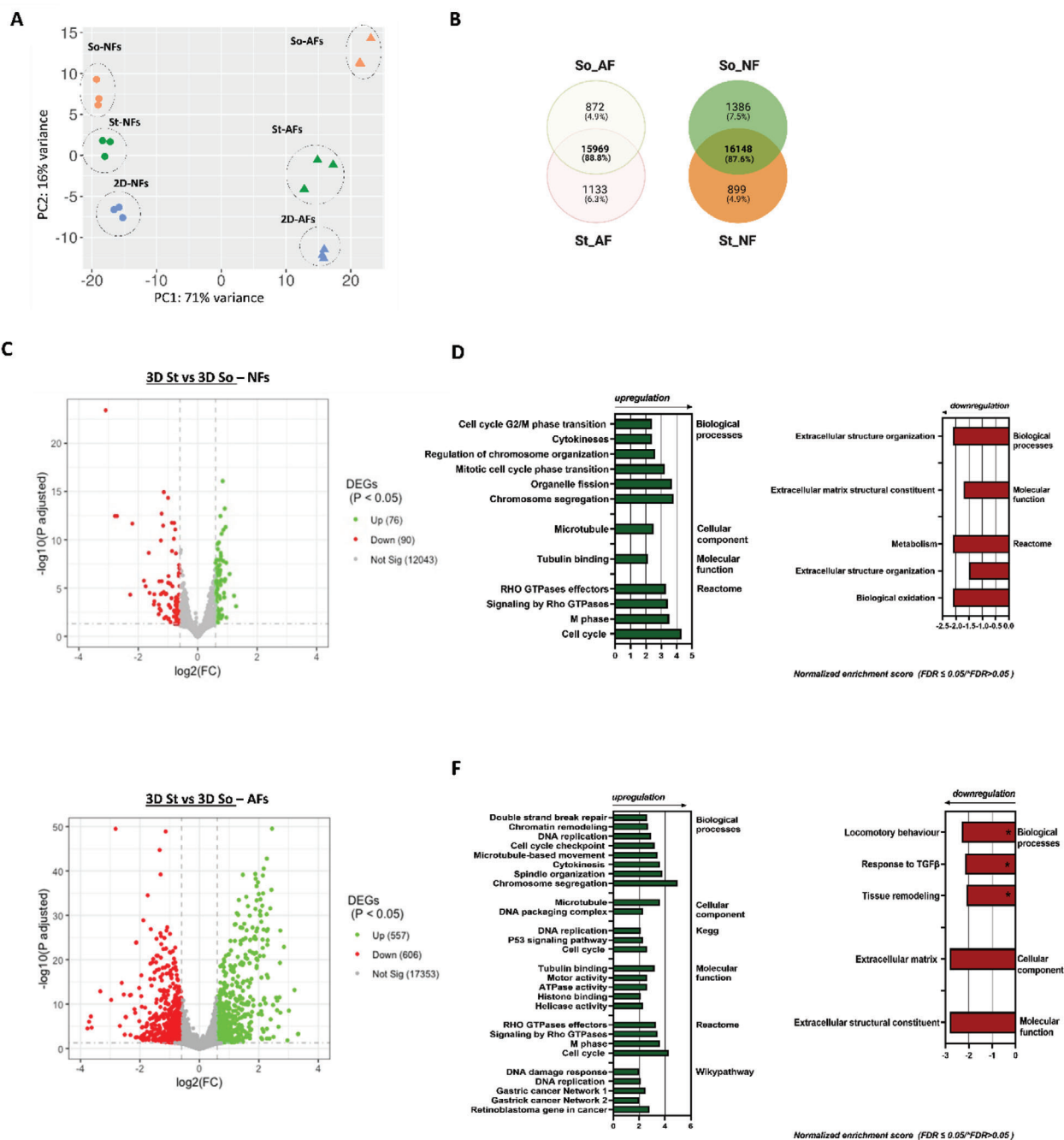
ADVANCED
SCIENCE NEWS

www.advancedsciencenews.com

{M} acro-
olecular
Bioscience

www.mbs-journal.de

Figure 6. AF gene expression is impacted by St culturing, activating many DNA-related pathways. A) Principal component analysis (PCA) of each biological replicate/condition. B) Venn diagram of genes unique and in common between AFs and NFs grown in So and St scaffolds. C) Volcano plot of NFs grown on St versus So. D) Differential analysis of gene expression pathways upregulated (left) and downregulated (right) in NFs grown on St versus So. (FDR < 0.05). E) Volcano plot of AFs grown on St versus So. F) Differential analysis of gene expression pathways upregulated (left) and downregulated (right) in AFs grown on St versus So (FDR < 0.05).
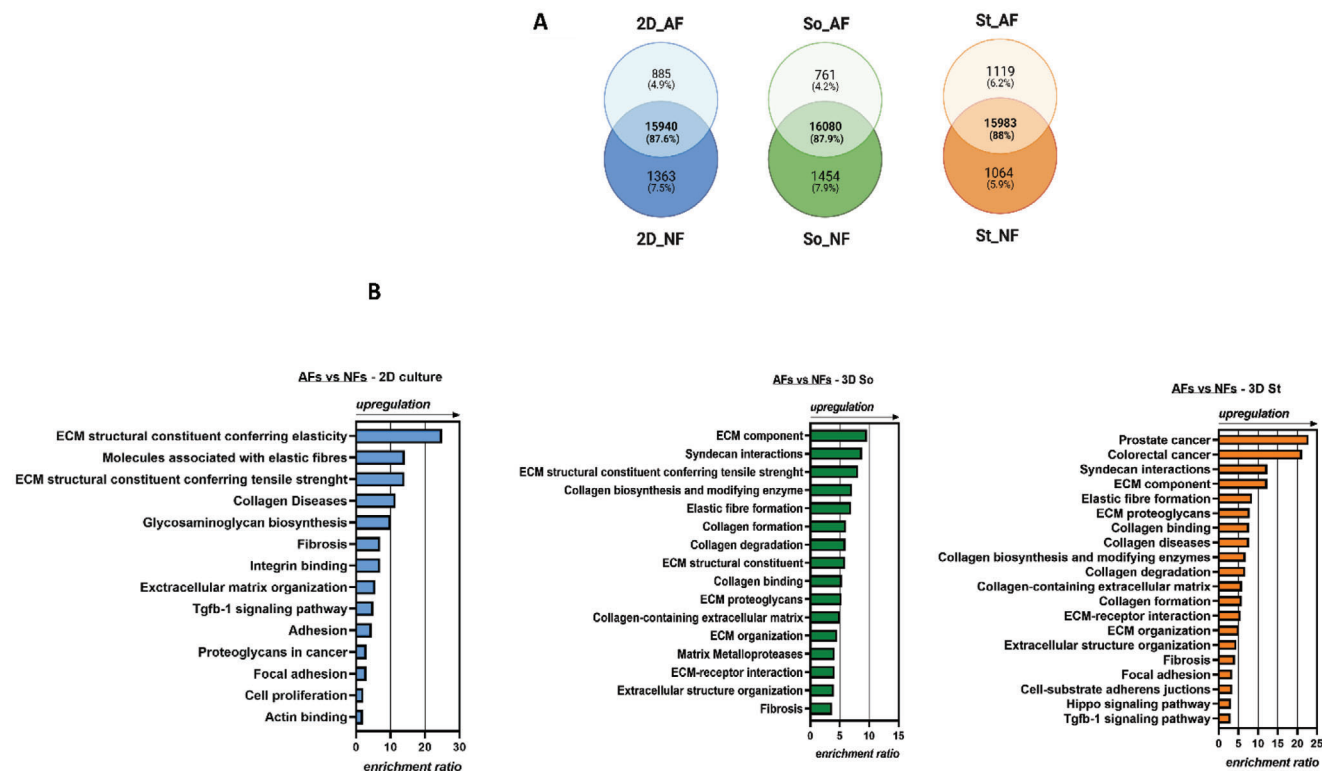
ADVANCED
SCIENCE NEWS
www.advancedsciencenews.com

Macro-
molecular
Bioscience
www.mbs-journal.de

Figure 7. Stiffer substrate impacts AF remodeling functions and promotes DNA replication and DNA repair and replication-related pathways. A) Venn diagram of genes counts unique and in common between 2D-grown AFs and NFs, So-grown AFs and NFs, and St-grown AFs and NFs. B) Differential analysis of gene expression pathways upregulated in AFs versus NFs on different culturing substrates.

many more differentially expressed genes in AFs, showing 557 upregulated and 606 downregulated genes on St compared to So ($p < 0.05$; Figure 6E). Among them, both NFs and AFs grown on St showed an upregulation of pathways such as regulation of chromosome organization and segregation, microtubules, cell cycle, signaling by Rho GTPases, and central regulators of actin reorganization, and consequently, function in cellular processes such as cell migration, wound healing, cell adhesion, cell polarity, membrane trafficking, and cytokinesis.[56,57] On the other side, both showed a downregulation of ECM constituents and organization (Figure 6D,F).

Of note is the characteristic response of AFs on St materials compared to So. The changes among the upregulated genes are more pronounced and involve DNA replication, DNA damage responses like double-strand break repair, and mitosis-related pathways like cytokinesis, M phase, and cell cycle enrichment. Interestingly, upregulation of genes related to gastric cancer and retinoblastoma were only found in AFs under St culturing, with a loss of ECM-related functions and downregulation of locomotory behavior, tissue remodeling, and extracellular constituent gene-related pathways (Figure 6F). In line with those observations, we further compared AF and NF profiles under different culturing conditions, trying to shed light on the underlying characteristic patterns that sensitize AFs to St substrates compared to NFs.

We investigated the effect of fibroblast activation at the gene expression level on each substrate. In the whole gene dataset, we recorded a higher number of unique genes expressed by NFs on both 2D and So materials compared to AFs (2D:1363, 7.5% of total; So:1454, 7.9% of total); a more even distribution of those genes was found on St materials for both NFs (1064, 5.9% of total) and AFs (1119, 6.2% of total) (**Figure 7**A), suggesting two distinct traits, but equivalent in number of genes, acquired by NFs and AFs on St scaffolds.

A deeper analysis comparing AF versus NF gene expression profiles on each substrate was performed to unveil how the cytokine activation effect could be amplified or weakened by the mechanical nature of the substrate. 2D cultured AFs acquired a typical functional state related to upregulation of ECM structural constituents as the top upregulated gene pathways in our analysis, conferring elasticity and tensile strength. As expected, AFs grown on 3D So scaffolds showed an upregulation of genes related to ECM component degradation and synthesis, ECM remodeling, but also elastic fiber formation and matrix metalloproteases, suggesting an active contractile phenotype acquisition and enzyme-dependent ECM degradation (Figure 7B and Figure S8, Supporting Information). Similar to what was observed on So scaffolds, AFs grown on St showed an upregulation of syndecan interactions pathways, a coreceptor recognized to promote liver and cardiac fibrosis[58] and an upregulation of ECM-related pathways mainly related to collagen remodeling, i.e., collagen binding/degradation/formation but also biosynthesis and modification. Interestingly, AFs grown on St scaffolds showed specific upregulation of gene expression pathways related to pathological diseases, spanning from fibrosis and collagen diseases to prostate

and colorectal cancer (Figure 7B and Figure S7, Supporting Information).

3. Discussion

The close relationship between fibrosis and the progression of solid tumors is well documented. Tumors, in particular carcinomas, activate, exaggerate, and prolong the latent wound-healing program of the host tissue,[59–61] resulting in a tumor niche that resembles a site of chronic wound healing.[62] The mutual presence of myofibroblastic cells, referred to here as activated fibroblasts with smooth-muscle-like features, have emerged as a particularly common hallmark of this close relationship.[63,64] AFs play a role in the synthesis of ECM and in force generation, resulting in ECM reorganization, wound contraction, and, importantly, altered tissue mechanics driven by altered fibrin, fibronectin, and collagen crosslinking and rearrangement.[65] Collagen crosslinking in particular has been shown to accompany tissue fibrosis that increases the risk of malignancy.[66–68]

In the present study, we mimicked mechanical and tensional features of normal and pathological tissue to explore how ECM stiffness may affect NF and AF phenotypes, behavior, and gene expression profiles. Already an elective platform in tissue engineering, we utilize highly porous permeable scaffolds in the broader spectrum of cancer research. Although not a focus in this study, such scaffold structures provide appropriate void spaces for mass transport and neovascularization. Importantly here, the collagen scaffolds act as a template for de novo tissue formation with tunable mechanical features.[69] For this reason, we employed a freeze-drying technique while employing BDDGE as crosslinking strategy to produce bovine collagen type I-based interconnected porous structures with controlled and reproducible porosity and fiber organization, resulting in a tunable system for 3D mechanical studies.[50,70,71]

In a native tissue context, cells are exposed to a variety of mechanical stimuli including hydrostatic pressure, shear, compression, and tensile force.[72] For this reason, soft biological tissues can be described as viscoelastic materials. Viscoelastic fluids (such as biological materials, known also as Bio-Soft-Matter) exhibit the characteristics of both a viscous fluid and an elastic solid.[73] To fully characterize the mechanical components of our model, we coupled micrometer-scale Young's Modulus analysis using AFM with a bulk assessment of scaffold viscous/elastic properties using shear rheometry. Overall, St scaffolds showed significantly higher Young's and shear modulus values compared to So, replicating the in vivo mechanical stiffness reported for many tumors such as breast and colon.[53] As a result, we were able to recreate the mechanical differences in the collagen matrix reported between diseased tissue (St; 1% BDDGE) and corresponding native tissue (St, 0.01% BDDGE), mimicking tissue fibrosis and desmoplastic areas.[74–78] Scaffold pore size and interconnectivity, as well as mechanical rigidity, have been shown to affect cell attachment.[79] In our So and St scaffolds, even if the pore sizes are significantly different, they span a range of optimal cell adhesion.[80,81] Furthermore, we can exclude that cell migration could be affected by the recorded pore sizes since they do not fall within a size range that would limit cell migration by physical arrest, based on previous studies.[82]

We selected MRC5 cells as the fibroblast cell line and activated them with a cytokine profibrotic factor TGFβ1, to promote AF activation as confirmed by the expression of two known biomarkers: FAP[83] and α-SMA.[84] MRC5 cells were previously used for both fibrosis studies (e.g., lung fibrosis[85,86]) and stroma/desmoplastic response studies (e.g., ovarian cancer,[87] liver cancer,[88] pancreatic cancer,[89] hepatocellular carcinoma[90]); while TGFβ1 is routinely used as a master regulator of fibrosis[91,92] and as proinflammatory tumor microenvironment signal to promote CAF activation.[87,93] Among the activation biomarkers used, FAP is a type II cell surface serine protease expressed by fibroblastic cells in areas of active tissue remodeling such as tumor stroma and healing wounds.[94,95] Furthermore, fibroblasts isolated from chronic fibrotic tissues are known to typically express higher α-SMA levels, leading to an increased contractility and cellular morphological change.[96] Noteworthy is that α-SMA+ fibroblast infiltration was significantly increased in the tumor stroma compared with that in benign breast tissue expression and correlated significantly with larger tumor size.[97]

In addition, employing 3D platform analysis enabled many features of the AF phenotype recorded in vivo to be studied in vitro. Using 2D substrates limits studies of cellular behavior such as migration and active contractility. Specifically, cell movement and differentiation occurs in response to environmental stimuli with the aim of achieving appropriate physiological outcomes; i.e., when stimuli are mechanical, cells can sense substrate stiffness through probing and contraction of actin fibers.[38] In human fibrotic organs, fibroblasts show increased ability to obtain a migratory phenotype.[98] Within tumors, peritumoral CAF migration and accumulation is often associated with increased deposition of ECM components in desmoplastic areas.[99] It has been suggested that CAFs in those areas are capable of executing a migratory program, characterized by accelerated motility and collective motility configuration, promoting cancer migration.[100–102] In our model, the softer So material was the only environment where both NF and AF cell migration was promoted, unveiling different migratory patterns for AFs and NFs. The directions of AF tracks converged to the center of the So scaffold whereas NFs did not show specific directionality.

Migration and ECM remodeling can also depend on contractile forces exerted by fibroblasts themselves.[103] In tumor settings for example, CAFs most proximal to the cancer cells usually exhibit a myofibroblasts phenotype and are highly contractile.[30,104] Indeed, NFs and AFs cultured on So showed significant reduction in scaffold diameter size during 7 d of culture, with a more pronounced shrinking effect of AFs, indicating a higher contractility phenotype for AFs than NFs on So materials. Tissue contraction mediated by AFs is considered the most important cause of increased interstitial pressure, which strongly delays drug delivery to cancer tissues.[105] Such increased contraction forces resulted in a decreased storage modulus after 7 d of AF culture on So, suggesting that in the early stages of both fibrotic and desmoplastic responses, AF activation does not result in higher stiffness. At the cellular level, cells sense and respond to the altered mechanical forces, for example through YAP mechanosensing, as shown in our stiffer St models, in turn driving the expression of a wide range of genes associated with AFs.[106,107] Within the softer So scaffold, however, we speculated that the observed

**ADVANCED
SCIENCE NEWS**

www.advancedsciencenews.com

Macro-
molecular
Bioscience

www.mbs-journal.de

cellular response may reproduce an early nesting or niche environment where cancer cells could migrate, grow, and proliferate rapidly. Alternatively, So scaffolds may mimic an early stage of the healing process, i.e., the granulation phase, where myofibroblasts (activated collagen secreting, α-SMA+ fibroblasts) are responsible for facilitating wound closure both by tractional forces and contraction.[108,109]

The whole-transcriptome RNA analysis clearly confirmed that the surrounding matrix stiffness can promote differential gene expression landscapes, especially in AFs. AFs on the So scaffold seemingly acquired a proremodeling phenotype, with higher z-score values of collagen and fibronectin, coupled with higher integrin expression, TGFβ1 amplification, and matrix metalloproteinase (MMPs) expression (Figure S7, Supporting Information). The stiffer (12-kPa) scaffold, St, resulted in an arrest in contractility, remodeling, and active AF phenotype alongside an enrichment of pathways related to DNA replication, chromatin remodeling, and cell cycle control. Also noteworthy was the upregulation of gene expression pathways related to pathological diseases in AFs compared with NFs, spanning from fibrosis and collagen-related conditions to prostate and colorectal cancer (Figure 7B). Such AF phenotypes, promoted only on a stiff 3D microenvironment, seemingly support the suitability of the St scaffold model to mimic disease states and also reinforce the notion of common ground between activated stroma in both fibrosis and the cancer microenvironment.

The wide-ranging matrix-, cellular-, and molecular-resolution findings of this study reinforce the importance of studying both NF and AF phenotypes in 3D, biologically relevant environments. As a platform for drug testing and basic tumor microenvironment research, such porous collagen scaffolds lend themselves to scalable, affordable expansion. As we demonstrated, AFs are strongly affected by substrate rigidity, shifting their gene expression profile to promote DNA replication and DNA repair-related pathways, an interesting phenotype not yet fully described and investigated in such reproducible in vitro 3D model systems. Further investigations may address important questions such as whether it is possible to tune myofibroblast fate, reprogramming stromal tissue inhabitant cells in favor of a "healing" tissue rather than a pathological one. Furthermore, could this be achieved through manipulating ECM parameters such as mechanical stiffness or identifying molecular pathways that promote ECM reorganization, altering the niche environment, thereby sensitizing stromal cells to reprogramming? If employed in certain niche environments, the introduction of highly controlled, 3D culture systems may begin to overcome clinical challenges in both fibrosis and cancer tumorigenesis/metastasis.

As a therapeutic strategy, targeting the effectors of myofibroblast activation, deactivation, and fate programs is one option.[110–113] We could also inhibit myofibroblast intracellular (contraction) or extracellular (stiffness and strain) stress as another promising approach to suppress myofibroblast activation or to drive myofibroblasts into controlled suicide.[114,115] Furthermore, ECM remodeling and crosslinking factors, such as matrix metalloproteases and lysyl oxidases, could be targeted to change ECM mechanics.[116–119] As previously shown, reprogramming cell-specific lineages is possible with the addition of soluble induction factors, but, as shown here, cells can change their expression profile and acquire a specific lineage due to the stiffness

and elasticity of their local, matrix environment. For example, soft matrices that mimic brain are neurogenic, stiffer matrices that mimic muscle are myogenic, and comparatively rigid matrices that mimic collagenous bone prove osteogenic.[120] In our model, AFs grown on 3D So materials can provide an effective and meaningful tool to explore tissue biological and biophysical changes and related ECM modifications occurring in first stages of fibrosis and tumor desmoplastic responses, whereas St materials could represent a snapshot of a late-stage fibrotic tissue, where stromal cells enter a "twilight" zone.[121–123] Testing therapeutics on this platform could be helpful to highlight potential antifibrotic drugs and/or to study AFs plasticity in response to microenvironment mechanical reprogramming.

4. Conclusion

Cells respond to alterations in the mechanical properties of their external surroundings by adjusting their intracellular tension through the cytoskeletal network, while signaling external changes to the nuclei, in turn affecting gene expression profiles. At the same time, intracellular tension changes result in alterations in ECM reorganization, thereby changing the mechanical properties of the matrix.[124] We employed a natural polymer collagen type I biomaterial scaffold to investigate mechanical alterations and track their effect on stromal cells in a 3D model that mimicked microenvironment mechanical dysfunctions observed in pathological conditions such as fibrosis and cancer. Using sponge scaffolds, we controlled the porosity and organization of the material and tested its stiffness and viscoelastic properties, reporting how changes in collagen crosslinking strongly impact the phenotype of AFs in a 3D setting, providing a meaningful platform to investigate both early and late stages of fibrosis and tumor dysplasia.

5. Experimental Section

Scaffold Preparation: Chemicals were purchased from Sigma-Aldrich. The scaffolds were synthesized from type I bovine collagen (Viscofan) and fabricated with the freeze-dry technique. Briefly, an acetic collagen slurry (200 mg mL^{-1}) was prepared, which was precipitated to a pH of 5.5 with NaOH (2 N). The slurry was wet crosslinked in an aqueous solution of 0.01 wt% (So) and 1 wt% (St) BDDGE at 4 °C for 24 h. Finally, the slurry was washed with Milli-Q water (Merk Millipore) and casted onto a 48-well plate and freeze dried through an optimized freezing and heating ramp (from 25 to −25 °C and from −25 to 25 °C in 50 min under vacuum conditions, $p = 0.20$ mbar) to obtain the desired pore size and porosity.

Atomic Force Microscopy: The atomic force microscope used in this experiment was the Bio-Catalyst AFM (Bruker). A spherical cantilever (Novascan) was used for the force measurement. A silica bead (5 μm in diameter) was mounted on to the end of the cantilever. The spring constant of the cantilever was 0.06 N m^{-1}. Before the AFM experiment, both the spring constant and sensitivity of the cantilever were calibrated under thermal tune conditions with the controlling software (Catalyst Nanoscope 8.15 SR3R1, Bruker). For the AFM experiment, scaffolds were embedded in optimal cutting temperature compound (OCT) and cryosectioned at 20 μm section thickness. The samples were precoated on a glass slide and kept under −80 °C. Then, samples were carefully moved into a 60 mm dish on the AFM scanning stage. A volume of 3 mL phosphate-buffered saline (PBS) or media was preinjected into the dish after sample incubation for 5 min at room temperature. For force measurement, the ramping size was kept at 10 μm. All experiments were conducted at room temperature (22 °C). Young's modulus was calculated from the force curves

with NanoScope Analysis 1.40 (Bruker). In the experiment, three to five spots were randomly tested per sample and recorded, and at least 50 force curves were acquired from each spot. In Young's modulus calculations, extended ramp force curves and a linearized model (spherical) were used.

Rheology: Wet and dry scaffolds of 1 mm thickness and 8 mm diameter were analyzed using an Anton Paar/MRC 302 rheometer equipped with an aluminum 8 mm insert plate. Both empty scaffolds and cellularized scaffolds collected at day 7 were characterized. An amplitude sweep test (log ramp 0.001%/10%, angular frequency of 10 Hz, 25 recorded points, T of 37 °C) was used to verify the range of linear viscoelasticity. Frequency response was measured by frequency sweep tests in the range 1000/0.1 rad s^{-1} (shear strain of 0.1%, 40 data points, T of 37 °C). Storage modulus and loss moduli measures were reported as three-sample averages collected at 1 rad s^{-1} angular frequency. Cellularized scaffold analyses were reported after normalization of both storage and loss moduli on D0 samples.

Scanning Electron Microscopy: The morphology of the scaffold was characterized by SEM and the pore size determined by ImageJ (US National Institutes of Health). Scaffolds were coated by 7 nm of Pt/Pl (Nova NanoSEM 230) for SEM examination. The pore diameter of scaffolds was measured from SEM images, and three images from each of three areas were used for each scaffold at the same magnification. For each image, porosity analysis was performed using "analyze particles" measurement in ImageJ software.

Fourier Transform Infrared Spectroscopy: The samples were analyzed in transmission mode at resolution 4, 64 points, over the range of 500–4000 cm^{-1} using a Nicolet 6700 spectrometer (Thermo-Fisher Scientific, Waltham, MA, http://www.thermofisher.com). The FTIR spectra were reported after background subtraction and baseline correction and reported on the graph within the range of 500–1800 cm^{-1}.

Thermal Gravimetric Analysis: The thermal stability and composition of St and So scaffolds (1% and 0.01% BDDGE) were analyzed by TGA under nitrogen atmosphere using a Mettler Toledo TGA/differential scanning calorimetry (DSC) 1 instrument. A temperature ramp from 25 to 800 °C with a heating rate of 10 °C min^{-1} was used to determine the onset decomposition temperatures. Approximately 10 mg samples were used.

Water Contact Angle (WCA) Measurement: The wettability of St and So scaffolds was assessed through WCA measurements using an Attension Theta optical tensiometer from Biolin Scientific. PBS droplets of 20 µL were deposited on the scaffold's surface and sessile drop measurements were performed. Side-view images of the deposited droplets were captured using the OneAttension software. The static contact angle formed by the droplet on the dry scaffold's surface was described using Young–Laplace equation. Scaffold wettability was observed for 10 min, evaluating the WCA every 2.15 s, and the data were reported as a mean of the CA at 10 min.

Cell Culture: MRC5 cells were purchased from American type culture collection (ATCC). Cultures were established in standard media constituted by Dulbecco's Eagle medium supplemented with 10% fetal bovine serum and 1% penicillin (100 UL mL^{-1})-streptomycin (100 mg mL^{-1}). For maintenance of cultures, cells were plated at a cell density of 3×10^3 cells per cm^2 and incubated at 37 °C in a humidified atmosphere (90%) with 5% CO$_2$. Medium was changed twice per week thereafter or according to the experiment requirements with the addition of TGFβ1. TGFβ1 titration was performed using increasing dose of TGFβ1 (0–50 ng mL^{-1}) and analysis performed at days 5 and 7. After establishment of 25 ng mL^{-1} as an elective dose for CAF activation, all further experiments used 25 ng mL^{-1} concentration and analysis performed after 7 d of culture. Adherent cells were detached from plates using Trypsin before reaching confluence (80%) and subsequently replated for culture maintenance. When seeded onto scaffolds, MRC5 cells were harvested and resuspended in cell culture medium. A 20 µL drop of medium containing 1×10^5 cells was seeded on the center of each scaffold (So and St) and kept in an incubator for 30 min. Culture medium was then added to each well.

H&E Staining: Hematoxylin and eosin staining was performed using the ST Infinity H&E Staining System (Leica Biosystems) in Leica Autostainer ST5010 XL. Paraffin was melted prior to staining by heating the slides at 60 °C for 30 min then slides were deparaffinized by performing 3×2 min washes in xylene, 3×1 min washes in 100% ethanol, and

1×1 min wash in 95% ethanol before rinsing in tap water. Slides were incubated for 30 s in Hemalast, for 5 min in hematoxylin, and were rinsed for 1 min in tap water. Next, slides were incubated for 30 s in Differentiator and 1 min in Bluing agent, with each step followed by a tap water rinse 1 min then 95% ethanol for 1 min. Slides were stained with eosin for 30 s, dehydrated in 95% ethanol for 1 min, 4 min in 100% ethanol, and 2×1 min in 100% ethanol, and cleared for 3×2 min in xylene. Every step after the initial heating of the slides was done at room temperature.

Flow Cytometry: *Monitoring Live–Death Percentage by Flow Cytometry Staining*: After 7 d of TGFβ1 treatment, scaffolds were incubated for 10' in Trypsin under shaking conditions, then scaffolds were removed and cells pellet was collected after centrifugation and washed with PBS. Cells were incubated with 2 µL of 50×10^{-6} M calcein acetoxymethyl ester (AM) working solution and 4 µL of ethidium homodimer-1 stock and incubated for 20 min at 37 °C protected from the light. After several washes with warm media, cells were analyzed by flow cytometry using BD fluorescence-activated cell sorting (FACS) Fortessa.

Propidium Iodide: After 7 d of TGFβ1 treatment, scaffolds were incubated for 10' in Trypsin under shaking conditions, then scaffolds were removed and cells pellet was collected after centrifugation at $500 \times g$ for 5 min and incubated overnight at 4 °C with 1 mL cold 70% ethanol. After adding PBS, cells were centrifuged and pellets resuspended in 1 mL of 0.1% Triton X-100/PBS containing 20 µL of 1 mg mL^{-1} propidium iodide and 10 µL 20 mg mL^{-1} RNase for 15 min at 37 °C. After washing with PBS, cells were resuspended in 300 µL of PBS and cell cycle analysis was performed by flow cytometry using BD FACS Fortessa.

CellTracker Green CMFDA Dye: After 7 d of TGFβ1 treatment, scaffolds were incubated for 10' in Trypsin under shaking conditions, then scaffolds were removed and cells pellet was collected after centrifugation and washed with PBS. Cells were incubated with CMFDA dye (1×10^{-6} M) for 20 min at 37 °C protected from the light. After several washes with warm media, cells were incubated for 10 min in fresh media before proliferation analyses were performed by flow cytometry using BD FACS Fortessa.

FAP Expression Quantification: After 7 d of TGFβ1 treatment, scaffolds were incubated for 10' in Trypsin under shaking conditions, then scaffolds were removed and cells pellet was collected after centrifugation and washed with 1% goat serum in PBS. Cells were incubated with FAP-PE (FAB37159) for 30 min at 37 °C protected from the light. After several washes with 1% goat serum in PBS, cells were analyzed by flow cytometry using BD FACS Fortessa.

Western Blot: Cells grown on 2D plates were collected after 7 d of TGFβ1 treatment using trypsin. After quenching with fresh media and washing with PBS, cells were suspended in radioimmunoprecipitation assay buffer (RIPA) buffer (89901, Thermo Fisher) and Protease Inhibitor Single-Use cocktail (100x) (78425, Thermo Fisher) and incubated for 15 min on ice. After bicinchoninic acid (BCA) quantification, 10 µg protein was loaded in each gel lane (Mini PROTEAN TGX GELS Cat# 4561096, 4–20%, Biorad). After protein transferring using Trans-Blot Turbo Transfer Pack (Cat# 1704158), membranes were blocked in 5% fat milk (TBS-Tween 0.1%) for 1 h and then incubated with primary antibodies: αSMA (ab5694, 1:1000) and GAPDH (ab9485, 1:1000) overnight. Secondary α-rabbit-horseradish peroxidase (HRP) was used (A16110, Invitrogen 1:1000) and membranes developed using ChemiDoc XRS+ (X-Ray Sensitivity, Biorad).

Microscopy: *Scaffold Shrinking*: Cells were seeded on both St and So scaffolds and imaged every day over a 7 d period using Keyence BZX800 with a 4x objective and performing a stich process to record the entire scaffold surface. Scaffold diameter analysis was performed using ImageJ. Relative scaffold shrinking was measured as the ratio of the diameter of after 7 d of culture with MRC5 cells to the diameter at day 1.

α-SMA Quantification: After 7 d of TGFβ1 treatment, cells were collected, centrifuged, and washed with 1% goat serum in PBS. After fixation with 4% paraformaldehyde for 10 min at room temperature, cellularized scaffolds were permeabilized using Triton X-100 0.1% in PBS for 10 min at room temperature. After washes, blocking was performed using 1% bovine serum albumin (BSA), 10% goat serum in PBS-Tween 0.1% for 30 min in a humified chamber at room temperature. Incubation with α-SMA-488 (ab197240, 1:250) was performed for 1 h at room temperature protected from light. 4',6-Diamidino-2-Phenylindole (DAPI) was added at

**ADVANCED
SCIENCE NEWS**

www.advancedsciencenews.com

Macromolecular
Bioscience

www.mbs-journal.de

300×10^{-9} M. Imaging was conducted with the Nikon A1 confocal imaging system, using a 40x objective and recording at least 3 z-stacks/scaffold.

Live–Death Imaging: Scaffolds were incubated with 2 µL of 50×10^{-6} M calcein AM working solution and 4 µL of ethidium homodimer-1 stock and incubated for 20 min at 37 °C protected from the light. After several washes with warm media, scaffolds were analyzed by Keyence BZX800 using a 4x objective and a final stich process to show the entire scaffold surface.

Live Imaging: After 7 d of TGFβ1 treatment, scaffolds were incubated with 2 µL of 50×10^{-6} M calcein AM working solution and incubated for 20 min at 37 °C protected from the light. DAPI was added at 10 µg mL^{-1}. MatTek Glass bottom microwell dishes were used for imaging. Live imaging of scaffold shrinking was performed using a Fluo View 3000 confocal microscope over 24 h with a 10x objective for 13 cycles at intervals of 2 h with a step size of 40 µm (slices: 20) for a total of 800 µm collected from the bottom of the scaffold. For cell migration tracking, analysis was performed over 24 h with a 10x objective for 13 cycles at intervals of 2 h, airy disk: 2, step size: 10 µm (slices: 43) and analyzed using Olympus cellSens software.

Fiber Orientation: OrientationJ is a software package which consists of a series of plugins for ImageJ and Fiji that automates orientation analysis. The program computes the local orientation and the local coherency. For each sample, six images were used as input of the structure tensor computation.

Reverse-Transcription Quantitative polymerase chain reaction (PCR): Reverse-transcription PCR was performed on cells grown on 2D plates, St scaffolds, or So scaffolds after 7 d. Cells were collected using trypsin, and after quenching with fresh media and washing with PBS, cells were suspended in lysis buffer and RNA extracted using RNeasy Mini Kit (Qiagen) according to the manufacturer's instructions. Total RNA (100 ng) was reverse transcribed into cDNA using Biorad iScript cDNA Synthesis Kit. Quantitative PCR was undertaken using TaqMan Fast Advanced Master Mix and performed on StepOnePlus (Real time PCR System, Applied Biosystems). Expression of *YAP* (Hs00902712), *WWTR1* (reported as TAZ, Hs00210007_m1), *MMP1* (Hs00899658), and *MMP2* (Hs01548727) was detected using TaqMan Gene Expression Assays. 18S ribosomal RNA was used as an internal reference for normalization. Analysis was performed using relative $\Delta\Delta C_t$ method.

RNA Sequencing: Library preparation and sequencing were carried out by Novogene (PE150). Raw fastq files were quality-checked using FastQC,[125] a quality-control tool for high throughput sequencing data. Reads were aligned to the GRCh38/hg38 genome build using spliced transcripts alignment to a reference (STAR).[126] Gene count tables were generated using the −quantMode GeneCounts argument in STAR. The DESeq2 median of means method[127] was used to normalize the gene count tables to account for sample depth. DESeq2 was used to correct for multiple hypothesis testing and determine significantly modified transcripts between control and experimental samples (false discovery rate (FDR) < 0.05). Raw and processed data are deposited in the gene expression omnibus (GEO) Database with accession number GSE168639. The platform WebGestalt was used to perform statistical overrepresentation analysis.[128] All major annotation sets were tested for overrepresentation by comparing the lists of genes expressed in different experimental conditions to those expressed by a standard genome of reference (FDR < 0.05). The lists of genes were compared using Venn diagrams through the Venny website.[129] Volcano plots were generated using the data visualization package ggplot2[130] within R.[131] Raw gene counts were normalized for all samples and replicates using the DEseq median of ratios method.[127] Normalized counts were then filtered to include only counts from genes of interest. The mean of the normalized counts for each replicate was calculated. The z-score of the averaged counts was calculated per gene, over all samples. The z-score heatmap was generated using ggplot2.[132] Analysis of DEGs was performed with a cutoff value fold change (FC) > |1.5|.

Statistical Analysis: All data were obtained from at least three independent experiments and expressed as mean $\pm$ standard deviation, with *n* indicating the number of replicates. The two-tailed Student's *t*-test with Welch's correction or ANOVA test was used to determine differences between groups. Results were considered to be statistically significant at P-value <0.05. The statistical analysis was processed with GraphPad Prism 6 Software (GraphPad; San Diego, CA, USA).

Conflict of Interest

The authors declare no conflict of interest.

Data Availability Statement

The data that support the findings of this study are available from the corresponding author upon reasonable request.

[1] T. R. Cox, *Nat. Rev. Cancer* **2021**, *21*, 217.

[2] M. J. Bissell, J. Aggeler, *Prog. Clin. Biol. Res.* **1987**, *249*, 251.

[3] B. Corradetti, F. Taraballi, C. Corbo, F. Cabrera, L. Pandolfi, S. Minardi, X. Wang, J. Van Eps, G. Bauza, B. Weiner, E. Tasciotti, *Sci. Rep.* **2017**, *7*, 17030.

[4] M. A. Karsdal, S. H. Nielsen, D. J. Leeming, L. L. Langholm, M. J. Nielsen, T. Manon-Jensen, A. Siebuhr, N. S. Gudmann, S. Rønnow, J. M. Sand, S. J. Daniels, J. H. Mortensen, D. Schuppan, *Adv. Drug Delivery Rev.* **2017**, *121*, 43.

[5] S. A. Eming, P. Martin, M. Tomic-Canic, *Sci. Transl. Med.* **2014**, *6*, 265sr6.

[6] N. C. Henderson, F. Rieder, T. A. Wynn, *Nature* **2020**, *587*, 555.

[7] T. A. Wynn, T. R. Ramalingam, *Nat. Med.* **2012**, *18*, 1028.

[8] A. Santos, D. Lagares, *Curr. Rheumatol. Rep.* **2018**, *20*, 2.

[9] J. D. Humphrey, E. R. Dufresne, M. A. Schwartz, *Nat. Rev. Mol. Cell Biol.* **2014**, *15*, 802.

[10] F. Paradiso, S. Serpelloni, L. W. Francis, F. Taraballi, *Int. J. Mol. Sci.* **2021**, *22*, 10098.

[11] S. Van Putten, Y. Shafieyan, B. Hinz, *J. Mol. Cell. Cardiol.* **2016**, *93*, 133.

[12] A. Angelini, J. Trial, J. Ortiz-Urbina, K. A. Cieslik, *Ageing Res. Rev.* **2020**, *63*, 101150.

[13] M. Paolillo, S. Schinelli, *Int. J. Mol. Sci.* **2019**, *20*, 4947.

[14] T. R. Cox, J. T. Erler, *Clin. Cancer Res.* **2014**, *20*, 3637.

[15] M. W. Pickup, J. K. Mouw, V. M. Weaver, *EMBO Rep.* **2014**, *15*, 1243.

[16] H. Breuninger, G. Schaumburg-Lever, J. Holzschuh, H. P. Horny, *Cancer* **1997**, *79*, 915.

[17] N. D. Ebelt, V. Zamloot, E. R. Manuel, *Oncotarget* **2020**, *11*, 3486.

[18] R. A. Walker, *Breast Cancer Res.* **2001**, *3*, 143.

[19] I. Acerbi, L. Cassereau, I. Dean, Q. Shi, A. Au, C. Park, Y. Y. Chen, J. Liphardt, E. S. Hwang, V. M. Weaver, *Integr. Biol.* **2015**, *7*, 1120.

[20] P. P. Provenzano, K. W. Eliceiri, J. M. Campbell, D. R. Inman, J. G. White, P. J. Keely, *BMC Med.* **2006**, *4*, 38.

[21] E. Brauchle, J. Kasper, R. Daum, N. Schierbaum, C. Falch, A. Kirschniak, T. E. Schäffer, K. Schenke-Layland, *Matrix Biol.* **2018**, *68–69*, 180.

[22] A. Neesse, H. Algül, D. A. Tuveson, T. M. Gress, *Gut* **2015**, *64*, 1476.

[23] V. Seewaldt, *Nat. Med.* **2014**, *20*, 332.

[24] E. J. Koay, Y. Lee, V. Cristini, J. S. Lowengrub, Y. Kang, F. A. S. Lucas, B. P. Hobbs, R. Ye, D. Elganainy, M. Almahariq, A. M. Amer, D. Chatterjee, H. Yan, P. C. Park, M. V. Rios Perez, D. Li, N. Garg, K. A. Reiss, S. Yu, A. Chauhan, N. Zaid, N. Nikzad, R. A. Wolff, M. Javle, G. R. Varadhachary, R. T. Shroff, P. Das, J. E. Lee, M. Ferrari, A. Maitra, C. M. Taniguchi, M. P. Kim, C. H. Crane, M. H. Katz, H. Wang, P. Bhosale, E. P. Tamm, J. B. Fleming, *Clin. Cancer Res.* **2018**, *24*, 5883.

[25] T. Liu, O. A. Babaniyi, T. J. Hall, P. E. Barbone, A. A. Oberai, *PLoS One* **2015**, *10*, e0130258.

[26] T. Wynn, *J. Pathol.* **2008**, *214*, 199.

[27] R. C. de Oliveira, S. E. Wilson, *Invest. Ophthalmol. Vis. Sci.* **2020**, *61*, 28.

[28] P. Pakshir, N. Noskovicova, M. Lodyga, D. O. Son, R. Schuster, A. Goodwin, H. Karvonen, B. Hinz, *J. Cell Sci.* **2020**, *133*, jcs227900.

[29] B. Hinz, S. H. Phan, V. J. Thannickal, M. Prunotto, A. Desmoulière, J. Varga, O. De Wever, M. Mareel, G. Gabbiani, *Am. J. Pathol.* **2012**, *180*, 1340.

[30] J. J. Tomasek, G. Gabbiani, B. Hinz, C. Chaponnier, R. A. Brown, *Nat. Rev. Mol. Cell Biol.* **2002**, *3*, 349.

[31] C. Ciobanasu, B. Faivre, C. Le Clainche, *Eur. J. Cell Biol.* **2013**, *92*, 339.

[32] S. Li, C. Li, Y. Zhang, X. He, X. Chen, X. Zeng, F. Liu, Y. Chen, J. Chen, *Theranostics* **2019**, *9*, 4993.

[33] N. A. Bhowmick, A. Chytil, D. Plieth, A. E. Gorska, N. Dumont, S. Shappell, M. K. Washington, E. G. Neilson, H. L. Moses, *Science* **2004**, *303*, 848.

[34] Y. Drabsch, P. Ten Dijke, *Cancer Metastasis Rev.* **2012**, *31*, 553.

[35] R. A. Evans, Y. A. C. Tian, R. Steadman, A. O. Phillips, *Exp. Cell Res.* **2003**, *282*, 90.

[36] S. Liu, J. Ren, P. Ten Dijke, *Signal. Transduction Targeted Ther.* **2021**, *6*, 8.

[37] K. Pietras, A. Östman, *Exp. Cell Res.* **2010**, *316*, 1324.

[38] R. Kalluri, M. Zeisberg, *Nat. Rev. Cancer* **2006**, *6*, 392.

[39] N. A. Bhowmick, E. G. Neilson, H. L. Moses, *Nature* **2004**, *432*, 332.

[40] F. Bonollo, G. N. Thalmann, M. Kruithof-de Julio, S. Karkampouna, *Cancers* **2020**, *12*, 1887.

[41] Y. Gao, Y. Yang, F. Yuan, J. Huang, W. Xu, B. Mao, Z. Yuan, W. Bi, *Oncogenesis* **2017**, *6*, e383.

[42] K. R. Levental, H. Yu, L. Kass, J. N. Lakins, M. Egeblad, J. T. Erler, S. F. T. Fong, K. Csiszar, A. Giaccia, W. Weninger, M. Yamauchi, D. L. Gasser, V. M. Weaver, *Cell* **2009**, *139*, 891.

[43] B. Piersma, M. K. Hayward, V. M. Weaver, *Biochim. Biophys. Acta, Rev. Cancer* **2020**, *1873*, 188356.

[44] G. Bassi, S. Panseri, S. M. Dozio, M. Sandri, E. Campodoni, M. Dapporto, S. Sprio, A. Tampieri, M. Montesi, *Sci. Rep.* **2020**, *10*, 22294.

[45] M. Zhang, P. Boughton, B. Rose, C. S. Lee, A. M. Hong, *Int. J. Biomater.* **2013**, *2013*, 396056.

[46] G. Rijal, W. Li, *J. Biol. Eng.* **2018**, *12*, 20.

[47] G. Bauza, A. Pasto, P. Mcculloch, D. Lintner, A. Brozovich, F. B. Niclot, I. Khan, L. W. Francis, E. Tasciotti, F. Taraballi, *Sci. Rep.* **2020**, *10*, 16610.

[48] F. Paradiso, J. Fitzgerald, S. Yao, F. Barry, F. Taraballi, D. Gonzalez, R. Steven Conlan, L. Francis, *Front. Bioeng. Biotechnol.* **2019**, *7*, 343.

[49] F. Taraballi, M. Sushnitha, C. Tsao, G. Bauza, C. Liverani, A. Shi, E. Tasciotti, *Adv. Healthcare Mater.* **2018**, *7*, 1800490.

[50] F. Taraballi, B. Corradetti, S. Minardi, S. Powel, F. Cabrera, J. L. Van Eps, B. K. Weiner, E. Tasciotti, *J. Tissue Eng.* **2016**, *7*, 204173141562466.

[51] N. I. Nissen, M. Karsdal, N. Willumsen, *J. Exp. Clin. Cancer Res.* **2019**, *38*, 115.

[52] R. G. Wells, *Biochim. Biophys. Acta* **2013**, *1832*, 884.

[53] P. Deptuła, D. Łysik, K. Pogoda, M. Cieśluk, A. Namiot, J. Mystkowska, G. Król, S. Głuszek, P. A. Janmey, R. Bucki, *ACS Biomater. Sci. Eng.* **2020**, *6*, 5620.

[54] X. Chen, S. L. Thibeault, *Tissue Eng., Part A* **2012**, *18*, 2528.

[55] M. Malumbres, M. Barbacid, *Nat. Rev. Cancer* **2009**, *9*, 153.

[56] S. J. Heasman, A. J. Ridley, *Nat. Rev. Mol. Cell Biol.* **2008**, *9*, 690.

[57] A. Hall, *Biochem. Soc. Trans.* **2012**, *40*, 1378.

[58] T. Parimon, C. Yao, D. M. Habiel, L. Ge, S. A. Bora, R. Brauer, C. M. Evans, T. Xie, F. Alonso-Valenteen, L. K. Medina-Kauwe, D. Jiang, P. W. Noble, C. M. Hogaboam, N. Deng, O. Burgy, T. J. Antes, M. Königshoff, B. R. Stripp, S. A. Gharib, P. Chen, *JCI Insight* **2019**, *4*, 333.

[59] B. L. Brücher, I. S. Jamall, *BMC Cancer* **2014**, *14*, 331.

[60] M. H. Barcellos-Hoff, D. Lyden, T. C. Wang, *Nat. Rev. Cancer* **2013**, *13*, 511.

[61] M. Schäfer, S. Werner, *Nat. Rev. Mol. Cell Biol.* **2008**, *9*, 628.

[62] B. Rybinski, J. Franco-Barraza, E. Cukierman, *Physiol. Genomics* **2014**, *46*, 223.

[63] P. Cirri, P. Chiarugi, *Am. J. Cancer Res.* **2011**, *1*, 482.

[64] C. Bonnans, J. Chou, Z. Werb, *Nat. Rev. Mol. Cell Biol.* **2014**, *15*, 786.

[65] G. Serini, G. Gabbiani, *Exp. Cell Res.* **1999**, *250*, 273.

[66] C. G. Colpaert, P. B. Vermeulen, S. B. Fox, A. L. Harris, L. Y. Dirix, E. A. Van Marck, *Breast Cancer Res. Treat.* **2003**, *81*, 137.

[67] S. Affo, L.-X. Yu, R. F. Schwabe, *Annu. Rev. Pathol.* **2017**, *12*, 153.

[68] D. Thomas, P. Radhakrishnan, *Mol. Cancer* **2019**, *18*, 14.

[69] B. A. Roeder, K. Kokini, J. E. Sturgis, J. P. Robinson, S. L. Voytik-Harbin, *J. Biomech. Eng.* **2002**, *124*, 214.

[70] E. Mondragón, M. Cowdin, F. Taraballi, S. Minardi, E. Tasciotti, C. A. Gregory, R. Kaunas, *Front. Bioeng. Biotechnol.* **2020**, *8*, 753.

[71] S. Minardi, B. Corradetti, F. Taraballi, M. Sandri, J. Van Eps, F. J. Cabrera, B. K. Weiner, A. Tampieri, E. Tasciotti, *Biomaterials* **2015**, *62*, 128.

[72] N. M. E. Ayad, S. Kaushik, V. M. Weaver, *Philos. Trans. R. Soc., B* **2019**, *374*, 20180215.

[73] D. T. Butcher, T. Alliston, V. M. Weaver, *Nat. Rev. Cancer* **2009**, *9*, 108.

[74] C. F. Guimarães, L. Gasperini, A. P. Marques, R. L. Reis, *Nat. Rev. Mater.* **2020**, *5*, 351.

[75] T. Yeung, P. C. Georges, L. A. Flanagan, B. Marg, M. Ortiz, M. Funaki, N. Zahir, W. Ming, V. Weaver, P. A. Janmey, *Cell Motil. Cytoskeleton* **2005**, *60*, 24.

[76] D. E. Discher, P. Janmey, Y.-L. Wang, *Science* **2005**, *310*, 1139.

[77] S. Kawano, M. Kojima, Y. Higuchi, M. Sugimoto, K. Ikeda, N. Sakuyama, S. Takahashi, R. Hayashi, A. Ochiai, N. Saito, *Cancer Sci.* **2015**, *106*, 1232.

[78] J. M. Goffin, P. Pittet, G. Csucs, J. W. Lussi, J.-J. Meister, B. Hinz, *J. Cell Biol.* **2006**, *172*, 259.

[79] I. Bružauskaitė, D. Bironaitė, E. Bagdonas, E. Bernotienė, *Cytotechnology* **2016**, *68*, 355.

[80] F. J. O'brien, B. A. Harley, I. V. Yannas, L. J. Gibson, *Biomaterials* **2005**, *26*, 433.

[81] I. V. Yannas, *Clin. Mater.* **1992**, *9*, 179.

[82] K. Wolf, M. Te Lindert, M. Krause, S. Alexander, J. Te Riet, A. L. Willis, R. M. Hoffman, C. G. Figdor, S. J. Weiss, P. Friedl, *J. Cell Biol.* **2013**, *201*, 1069.

[83] J. E. Park, M. C. Lenter, R. N. Zimmermann, P. Garin-Chesa, L. J. Old, W. J. Rettig, *J. Biol. Chem.* **1999**, *274*, 36505.

[84] X. Chen, E. Song, *Nat. Rev. Drug Discovery* **2019**, *18*, 99.

[85] O. Kayalar, F. Oztay, H. G. Ongen, *Cell Commun. Signaling* **2020**, *18*, 96.

[86] M. Huang, H. Yang, L. Zhu, H. Li, J. Zhou, Z. Zhou, *Environ. Toxicol.* **2016**, *31*, 1620.

[87] Z. Yang, S. Xu, P. Jin, X. Yang, X. Li, D. Wan, T. Zhang, S. Long, X. Wei, G. Chen, L. Meng, D. Liu, Y. Fang, P. Chen, D. Ma, Q. Gao, *Oncotarget* **2016**, *7*, 37649.

[88] S.-M. Ding, J.-F. Lu, M. I. A. Edoo, L. Zhou, H.-Y. Xie, S.-S. Zheng, Q.-Y. Li, *Int. J. Med. Sci.* **2019**, *16*, 1157.

[89] S.-M. Ding, A.-L. Lu, W. Zhang, L. Zhou, H.-Y. Xie, S.-S. Zheng, Q.-Y. Li, *J. Cancer* **2018**, *9*, 614.

[90] S. Ding, G. Chen, W. Zhang, C. Xing, X. Xu, H. Xie, A. Lu, K. Chen, H. Guo, Z. Ren, S. Zheng, L. Zhou, *J. Transl. Med.* **2015**, *13*, 237.

[91] A. Biernacka, M. Dobaczewski, N. G. Frangogiannis, *Growth Factors* **2011**, *29*, 196.

[92] X.-M. Meng, D. J. Nikolic-Paterson, H. Y. Lan, *Nat. Rev. Nephrol.* **2016**, *12*, 325.

[93] T.-L. Yeung, C. S. Leung, K.-K. Wong, G. Samimi, M. S. Thompson, J. Liu, T. M. Zaid, S. Ghosh, M. J. Birrer, S. C. Mok, *Cancer Res.* **2013**, *73*, 5016.

[94] T. Ramirez-Montagut, N. E. Blachere, E. V. Sviderskaya, D. C. Bennett, W. J. Rettig, P. Garin-Chesa, A. N. Houghton, *Oncogene* **2004**, *23*, 5435.

[95] A. A. Fitzgerald, L. M. Weiner, *Cancer Metastasis Rev.* **2020**, *39*, 783.

[96] L. Chadli, B. Sotthewes, K. Li, S. N. Andersen, E. Cahir-McFarland, M. Cheung, P. Cullen, A. Dorjée, J K. de Vries-Bouwstra, T. W. J. Huizinga, D. F. Fischer, J. DeGroot, J. L. Viney, T. S. Zheng, J. Aarbiou, A. Gardet, *Sci. Rep.* **2019**, *9*, 4521.

[97] K. Amornsupak, P. Jamjuntra, M. Warnnissorn, P. O-Charoenrat, D. Sa-Nguanraksa, P. Thuwajit, S. A. Eccles, C. Thuwajit, *Clin. Breast Cancer* **2017**, *17*, 441.

[98] Y.-Y. Lu, X.-K. Zhao, L. Yu, F. Qi, B. Zhai, C.-Q. Gao, Q. Ding, *Sci. Rep.* **2017**, *7*, 46357.

[99] L. A. Kunz-Schughart, R. Knuechel, *Histol. Histopathol.* **2002**, *17*, 599.

[100] J. O. Waldeland, W. J. Polacheck, S. Evje, *J. Biomech.* **2020**, *100*, 109568.

[101] B. Erdogan, M. Ao, L. M. White, A. L. Means, B. M. Brewer, L. Yang, M. K. Washington, C. Shi, O. E. Franco, A. M. Weaver, S. W. Hayward, D. Li, D. J. Webb, *J. Cell Biol.* **2017**, *216*, 3799.

[102] K. Miyazaki, J. Oyanagi, D. Hoshino, S. Togo, H. Kumagai, Y. Miyagi, *Sci. Rep.* **2019**, *9*, 292.

[103] S. C. Schwager, P. V. Taufalele, C. A. Reinhart-King, *Cell. Mol. Bioeng.* **2019**, *12*, 1.

[104] D. Öhlund, A. Handly-Santana, G. Biffi, E. Elyada, A. S. Almeida, M. Ponz-Sarvise, V. Corbo, T. E. Oni, S. A. Hearn, E. J. Lee, I. I. C. Chio, C.-I. Hwang, H. Tiriac, L. A. Baker, D. D. Engle, C. Feig, A. Kultti, M. Egeblad, D. T. Fearon, J. M. Crawford, H. Clevers, Y. Park, D. A. Tuveson, *J. Exp. Med.* **2017**, *214*, 579.

[105] C.-H. Heldin, K. Rubin, K. Pietras, A. Östman, *Nat. Rev. Cancer* **2004**, *4*, 806.

[106] E. Sahai, I. Astsaturov, E. Cukierman, D. G. Denardo, M. Egeblad, R. M. Evans, D. Fearon, F. R. Greten, S. R. Hingorani, T. Hunter, R. O. Hynes, R. K. Jain, T. Janowitz, C. Jorgensen, A. C. Kimmelman, M. G. Kolonin, R. G. Maki, R. S. Powers, E. Puré, D. C. Ramirez, R. Scherz-Shouval, M. H. Sherman, S. Stewart, T. D. Tlsty, D. A. Tuveson, F. M. Watt, V. Weaver, A. T. Weeraratna, Z. Werb, *Nat. Rev. Cancer* **2020**, *20*, 174.

[107] F. Calvo, N. Ege, A. Grande-Garcia, S. Hooper, R. P. Jenkins, S. I. Chaudhry, K. Harrington, P. Williamson, E. Moeendarbary, G. Charras, E. Sahai, *Nat. Cell Biol.* **2013**, *15*, 637.

[108] T. Mentzel, C. D. M. Fletcher, *Am. J. Clin. Pathol.* **1997**, *107*, 2.

[109] A. Desmoulière, I. A. Darby, G. Gabbiani, *Lab. Invest.* **2003**, *83*, 1689.

[110] A. Fintha, Á. Gasparics, L. Rosivall, A. Sebe, *Front. Pharmacol.* **2019**, *10*, 388.

[111] J. Franco-Barraza, D. A. Beacham, M. D. Amatangelo, E. Cukierman, *Curr. Protoc. Cell. Biol.* **2016**, *71*, 10.9.1.

[112] S. Yazdani, R. Bansal, J. Prakash, *Adv. Drug Delivery Rev.* **2017**, *121*, 101.

[113] Y. Tai, E. L. Woods, J. Dally, D. Kong, R. Steadman, R. Moseley, A. C. Midgley, *Biomolecules* **2021**, *11*, 1095.

[114] T. Kuehl, D. Lagares, *Matrix Biol.* **2018**, *68–69*, 94.

[115] A. J. Haak, E. Kostallari, D. Sicard, G. Ligresti, K. Moo Choi, N. Caporarello, D. L. Jones, Q. Tan, J. Meridew, A. M. Diaz Espinosa, A. Aravamudhan, J. L. Maiers, R. D. Britt Jr., A. C. Roden, C. M. Pabelick, Y. S. Prakash, S. M. Nouraie, X. Li, Y. Zhang, D. J. Kass, D. Lagares, A. M. Tager, X. Varelas, V. H. Shah, D. J. Tschumperlin, *Sci. Transl. Med.* **2019**, *11*, eaau6296.

[116] N. A. Afratis, M. Selman, A. Pardo, I. Sagi, *Matrix Biol.* **2018**, *68–69*, 167.

[117] A. D. Theocharis, D. Manou, N. K. Karamanos, *FEBS J.* **2019**, *286*, 2830.

[118] M. Walraven, B. Hinz, *Matrix Biol.* **2018**, *71–72*, 205.

[119] A. De Vita, C. Liverani, R. Molinaro, J. O. Martinez, K. A. Hartman, C. Spadazzi, F. Miserocchi, F. Taraballi, M. Evangelopoulos, F. Pieri, A. Bongiovanni, L. Mercatali, E. Tasciotti, T. Ibrahim, *Sci. Rep.* **2021**, *11*, 5107.

[120] A. J. Engler, S. Sen, H. L. Sweeney, D. E. Discher, *Cell* **2006**, *126*, 677.

[121] M. Schosserer, J. Grillari, M. Breitenbach, *Front. Oncol.* **2017**, *7*, 278.

[122] M. Mellone, C. J. Hanley, S. Thirdborough, T. Mellows, E. Garcia, J. Woo, J. Tod, S. Frampton, V. Jenei, K. A. Moutasim, T. D. Kabir, P. A. Brennan, G. Venturi, K. Ford, N. Herranz, K. P. Lim, J. Clarke, D. W. Lambert, S. S. Prime, T. J. Underwood, P. Vijayanand, K. W. Eliceiri, C. Woelk, E. V. King, J. Gil, C. H. Ottensmeier, G. J. Thomas, *Aging (Albany NY)* **2016**, *9*, 114.

[123] A. Krtolica, S. Parrinello, S. Lockett, P. Y. Desprez, J. Campisi, *Proc. Natl. Acad. Sci. U. S. A.* **2001**, *98*, 12072.

[124] D. T. Butcher, T. Alliston, V. M. Weaver, *Nat. Rev. Cancer* **2009**, *9*, 108.

[125] Andrews, S. (2010). FASTQC. A quality control tool for high throughput sequence data.

[126] A. Dobin, C. A. Davis, F. Schlesinger, J. Drenkow, C. Zaleski, S. Jha, P. Batut, M. Chaisson, T. R. Gingeras, *Bioinformatics* **2013**, *29*, 15.

[127] M. I. Love, W. Huber, S. Anders, *Genome Biol.* **2014**, *15*, 550.

[128] J. Wang, S. Vasaikar, Z. Shi, M. Greer, B. Zhang, *Nucleic Acids Res.* **2017**, *45*, W130.

[129] Oliveros, J.C. (2007-2015) Venny. An Interactive Tool for Comparing Lists with Venn's Diagrams.

[130] H. Wickham, *ggplot2: Elegant Graphics for Data Analysis*, Springer-Verlag, New York **2016**.

[131] R Core Team (2018). R: A language and environment for statistical computing. R Foundation for Statistical Computing, Vienna, Austria.

[132] H. Wickham, *ggplot2: Elegant Graphics for Data Analysis*, Springer Publishing Company, Incorporated, New York **2009**.